A Covert, Secure and Energy-Efficient Communication Protocol Based on Statistical Machine Learning in Multi-Domain Communication Applications

Sobhan Esmaeili[1], Jamal Ghasemi[2*]

[1]Faculty of Engineering and Technology, University of Mazandaran, Babolsar, Mazandaran, Iran

[2]Faculty of Engineering and Technology, University of Mazandaran, Babolsar, Mazandaran, Iran

Abstract

In recent years, multi-domain (air-water) optical wireless communication has gained wide scientific and civil interest for its versatile applications. However, in addition to security challenges, these types of communications face limitations regarding direct cross-medium communication, transmission capacity, transmission range, and energy consumption due to water properties and reflections occurring at the interface between the two mediums. In this research, we propose a secure covert communication protocol with energy efficiency for multi-domain communication applications to address the aforementioned challenges. In this protocol, to enhance security and reduce bandwidth consumption, data is sampled based on its entropy and then simultaneously compressed and encrypted according to its sparsity level. Next, the resulting output is modulated onto amplified spontaneous emission (ASE) noise, hidden, and spread out over time using a chirped fiber Bragg grating (CFBG). The signal is then transmitted through a wide-field optical system. Here, we utilize an array of ultrasonic sensors and a prediction algorithm to calculate the optimal water surface impact point. We

[1]Email: s.esmaeili@umail.umz.ac.ir | Tel: +98-21-22016579 | Mobile: +98-912-212-3203 | Postal Address: Faculty of Engineering and Technology, University of Mazandaran, Pasdaran Street, P.O, Babolsar, Iran.

[2]Email: j.ghasemi@umz.ac.ir | Tel: +98-11-35303000 | Mobile: +98-911-325-5892 | Postal Address: Faculty of Engineering and Technology, University of Mazandaran, Pasdaran Street, Babolsar, Iran.

[*]Corresponding Author

also optimize energy use and boost data capacity via laser diode switching with simple on-off keying (OOK) modulation. The simulation results demonstrate that the proposed model reduces energy consumption and increases transmission capacity compared to previous methods.

Keywords*:* Covert Communications, Secure Communications, Multi-Domain Communications, Energy-Efficient Communications, Statistical Machine Learning

1. **Introduction**

The paradigm of Multi-Domain Operations (MDO), with its emphasis on establishing integrated communications, has garnered significant attention from both scientific and industrial communities [1]. The implementation of this paradigm necessitates establishing secure, energy-efficient communications between systems across different domains (water, air) while maintaining optimal data transmission rates. However, since most existing wireless communication technologies primarily focus on a single physical environment, they are unable to penetrate physical boundaries such as air-water interfaces, resulting in degraded performance [2]. Traditional hybrid methods (e.g., optical-acoustic, TARF, relay-based) lack security, scalability, and efficiency due to limited data rates, high energy use, and mobility constraints, making them unsuitable for practical use [3–5]. These limitations have driven growing interdisciplinary research interest in recent years [6,7].

In [8], a location-aware covert communication protocol using a 320 nm laser and hybrid network is proposed to enhance BER, energy efficiency, and channel capacity. Despite its benefits, high costs and potential security risks in resource sharing limit its practicality. In [9], the authors propose a wireless communication system based on a 450-nm laser and an avalanche photodetector, enabling data exchange at short distances with data transmission rates of 6 to 10 Mbps. In [10], a covert water-to-air optical wireless communication method is proposed using a narrow signal waveband and avalanche photodiode nonlinearity to hide transmissions. A shared secret wavelength pattern guides signal transmission, aiming to maximize throughput while maintaining stealth. Despite its practicality and resource efficiency, the method faces challenges in data rate and secure pattern sharing, and its covertness may be compromised by optical filters at unauthorized receivers.

In [11], an adaptive beamforming method based on the state action reward state action (SARSA) algorithm was proposed to enhance underwater optical communication quality.

Although this algorithm demonstrates superior performance compared to static and random methods, it suffers from a long convergence time.

In [12], a covert water-to-air optical communication method using adversarial autoencoders (AAE) is introduced, which embeds secret data into transmitted signals without extra resources like Intelligent Reflecting Surface (IRS) or antennas. The AAE generates signals resembling artificial noise to confuse eavesdroppers, while legitimate receivers can decode the message. Although the method offers strong covertness and resilience under varying conditions, its demodulation error rate is slightly higher than that of linear block codes (LBCs). In [13], an optical wireless method using DDPG and EKF ensures reliable air-water communication between mobile agents. While energy-efficient and robust in dynamic conditions, it faces high computational complexity and reduced real-time performance in turbulent waters.

In [14], a real-time water-to-air optical wireless system using field programmable gate array (FPGA), multiple-input multiple-output (MIMO), and low-density parity check (LDPC) codes is introduced, offering low frame error rate (FER) under dynamic conditions. However, it lacks active tracking, relying on coarse alignment. In [15], a wide field-of-view (FOV) water-to-air optical camera communication (OCC) system using rolling-shutter (RS) and long short-term memory neural networks (LSTM-NNs) is proposed to handle water turbulence and decode 4-level pulse amplitude modulation (PAM-4) signals. While the system offers high data rates and robustness to water turbulence, its complexity and limited range pose challenges for practical deployment. Despite the growing use of wireless optical communication in multidisciplinary domains, existing solutions often lack sufficient security and face challenges related to energy efficiency, range, and capacity [16]. To address these gaps, this study targets covert, bi-directional air–water communication by designing a wavelength-conversion-based optical system operating in both detection and transmission modes. This system enables secure data exchange under LoS and NLoS conditions. The proposed model, developed under the assumptions listed in Table 1, simplifies protocol complexity while maintaining precision in addressing core challenges.

In the proposed system, to establish a secure and covert optical link, input data is entropy-sampled, compressed, and encrypted based on sparsity, then modulated onto ASE noise and time-dispersed using a Chirped Fiber Bragg Grating before transmission. OOK pulse modulation and high-speed laser switching enhance data rate and energy efficiency, while also

stabilizing laser temperature. To maintain SNR under strong ambient light, a narrow optical filter is used with a sensitive SiPM detector. A compact optical setup (combining MEMS mirrors, object-space imaging, and fisheye lenses) enables ±78° beam steering across 174° FOV. For adaptation to water surface dynamics, 12 frequency-diverse ultrasonic sensors with AI-based prediction and compressed sensing provide accurate wave profiling to guide optimal beam projection. The model's performance is validated via simulations and experimental evaluations. Key contributions include a secure, energy-efficient multi-domain communication protocol with improved range, capacity, and robustness under environmental challenges. The remainder of this paper is organized as follows: Section 2 briefly describes the optical system, its constituent components, and the water surface model. Section 3 details the proposed scheme. Section 4 presents the parameter settings used in the simulation. Section 5 analyzes and evaluates the simulation results. Finally, Section 6 concludes the paper and discusses future work.

2. **Optical system architecture and water surface modeling**

This section briefly describes the optical system architecture, its constituent components, and the water surface model employed in the communication protocol analysis.

2.1. Optical system

To enable robust air-water communication, a wavelength-adaptive optical system is developed using selectable laser sources (320 nm, 800 nm, and 1050-1540 nm) based on the operational mode and channel conditions. In detection mode, a low-power beam is emitted to locate targets, followed by data transmission via beam steering. The system uses 320 nm for Non-Line-of-Sight (NLoS) and longer wavelengths for Line-of-Sight (LoS), optimizing performance under varying atmospheric and environmental conditions while addressing concealment, range, and energy efficiency. These wavelengths, less affected by water absorption and ambient noise, reduce interference and detection risk. The system applies On-Off Keying (OOK) pulse modulation to balance rate and power without thermal control. At the receiver, a highly sensitive photodetector (SiPM) with a narrow bandpass filter enhances SNR, widens the field of view, and enables efficient photon detection. Fig. 1(a) and Fig. 1(b) illustrate the transmitter tracking structure and receiver optical setup, respectively.

As depicted in Fig. 1(a), the transmitter's tracking unit integrates a small-angle microelectromechanical (MEMS) mirror, object-space imaging, and a compact fisheye lens. To expand the beam directionality, the design (Fig. 2) redirects incident light from a 10° input angle to a 174° output by utilizing an imaging plane for beam divergence.

The fisheye lens system employs a mix of spherical/aspherical lenses with fewer elements and varied glass types to reduce size and weight while optimizing image quality via aberration control. In the tracking unit, an object-space imager corrects spherical aberrations and aligns the MEMS mirror output with the fisheye lens image plane for precise reverse-path propagation.

2.2. Water surface model

Given the complexity of factors affecting water surface waves [19,20], deriving a universal descriptive model is difficult. In this study, the cnoidal wave model (assuming constant amplitude, frequency, and mean level) is used to simulate shallow water waves and assess their effect on the proposed method [21]. Although this assumption may not always hold due to environmental variations, it provides a practical approximation. Fig. 3 depicts the resulting wave shape and height.

As can be seen in Fig. 3, the cnoidal waves have a longer crest and wider trough than the sine wave. Besides, in cnoidal waves, various parameters such as elevation, length, and speed of wave propagation can be determined. Therefore, the cnoidal wave model can be used as a good model for simulating and studying the behavior of water-surface waves due to its simplicity and high accuracy [22]. Using Eq. (1), the cnoidal wave model can be modeled as follows [30].

$$f(x,y,t)=\left[\frac{H}{m}-H-\frac{HE(m)}{mK(m)}\right]+HJ^{2}\left(\left(\left(\left(\frac{2K(m)\left[x-\left(\sqrt{gh}\left[1+\frac{0.5H}{h}-\frac{1.5HE(m)}{mhK(m)}\right]\right)t\right]}{\lambda_{w}}\right)\middle|m\right)\right)\right) \quad (1)$$

where, $f(x,y,t)$ is water surface elevation at a point with coordinates (x,y), at time t; H represents wave height; h denotes water depth; m is elliptic modulus parameter with values in range $[0,1]$; g is Earth's gravitational acceleration; λ_w is wavelength of water surface wave; and $K(m)$, $E(m)$ and J are respectively, complete elliptic integral of the first type, complete

elliptic integral of the second type and Jacobi's elliptic function, respectively, calculated according to the elliptic modulus.

3. **Proposed Method**

As highlighted in [23], the absence of a unified multi-domain communication protocol poses a major challenge. To address this, we propose a novel covert, secure, and energy-efficient protocol integrating emerging technologies to ensure reliable, seamless data exchange across heterogeneous domains. Key implementation stages are outlined in Fig. 4 and elaborated in subsequent sections.

3.1. Calculating sparsity and determining the compression ratio

At this stage, the receiving unit continuously monitors the received data and calculates its sparsity according to Eq. (2) [17,18].

$$S_X = \frac{\| X\|_1^2}{\| X\|_2^2} \tag{2}$$

In Eq. (2), SX represents the degree of data sparsity, while $\|X\|_1^2$ and $\|X\|_2^2$ represent the squared $\ell_1 - norm$ and the squared $\ell_2 - norm$ of vector X, respectively. Furthermore, vector X comprises the sum of the absolute values of the data received by the receiving unit.

Here, if the changes in data sparsity sensed are more than 50%, the receiver unit calculates and uses a new compression factor according to Eq. (3) [17,18] and the number of measurements calculated based on Eq. (4) [17,18]. If no specific compression ratio is specified, the receiving unit will employ the default setting. The number of measurements determining the compression factor is directly influenced by the sparsity of the received data.

$$\begin{cases} CR = CR_{Default} \; if \; 0 \le \Delta SX < 50\% \\ CR = \dfrac{M}{N} \; and \; M > 2SX \log_{10}^{\frac{N}{SX}} \; if \; \Delta SX \ge 50\% \end{cases} \tag{3}$$

$$M > 2SX \log_{10}^{\frac{N}{SX}} \tag{4}$$

In Eqs. (3) and (4), CR denotes the compression coefficient, $CR_{Default}$ is the default compression coefficient, ΔSX represents the change of the sensed data sparsity, M is the number of measurements and N is the number of samples.

3.2. Secure and lightweight sensing

In this step, data is sampled based on its information rate, requiring fewer measurements than dictated by Nyquist's theorem. A sparse sub-Gaussian matrix, designed as in Eq. (5) [17,18] and built from a shared random kernel between authorized underwater and air nodes, ensures secure data acquisition while minimizing cryptographic computations.

$$\begin{cases} P\left(\psi_{ij}=k\right)=\dfrac{1}{2SX} \\ P\left(\psi_{ij}=0\right)=1-\dfrac{1}{2SX} \end{cases} \tag{5}$$

Here, when the value of ψ_{ij} is zero, no encryption operation takes place, and when it is equal to k, the j^{th} underwater node/air node will display its i^{th} received data on the columns of the corresponding Ψ_i matrix to obtain its Y_i measurement result. The result of Y_i measurement is an encrypted message based on the Ψ_i matrix, and the eavesdropper is not able to read it; to recover it, the authorized underwater node/air node must have the matrix.

3.3. Detecting and tracking the target receiver

In this section, precise retroreflectors and a highly collimated laser beam are employed for passive sensing and localization. The transmitter, operating in discovery mode, emits a low-power laser until it is reflected by a retroreflector at the target node, enabling its localization through reflected beam analysis [24]. Upon detection, the system switches to data transmission, repeating this cycle to maintain alignment despite node mobility.

3.4. Depth sampling

3.4.1. Determining the shape of the water surface

To sample the water surface shape, an array of 12 ultrasonic sensors with varying heights is used to balance accuracy, complexity, and cost. As shown in Fig. 5, these sensors are distributed around a central laser diode. To enhance sampling precision and avoid interference or inefficiency with short-wavelength waves, a compressed sensing approach inspired by fuzzy logic [25] and frequency-diverse sensors is employed.

The compressed sensing technique recovers sparse high-dimensional signals using fewer measurements by projecting them onto a limited set of vectors, capturing only key informative

coefficients. This data-driven approach, guided by information content rather than the Nyquist rate, enables efficient sampling and discards irrelevant data. Its mathematical model is defined in Eq. (6) [17,18].

$$Min\left\|X_{sj}\right\|_1 S.T\, Y_{sj}\left[M\times 1\right]=\Psi_i\left[M\times N\right]\times X_{sj}\left[N\times 1\right]: j\in\left[1,12\right]\wedge i\in\left[1,n\right] \quad (6)$$

Here, Y_{S_j} is the vector of data sensed by sensor number j after compressed sensing, X_{S_j} denotes the vector of data sensed by j^{th} sensor number and Ψ_i is the measurement matrix of the the ith round.

3.4.2. Prediction of wave elevation

Since water surface waves are periodic, it is possible to reduce the latency caused by the measurement process by predicting the elevation of the water surface. Here, as multiple fundamental frequencies are assumed to exist in water waves, we use Auto Regressive Integrated Moving Averages (ARIMA) modeling to predict the water surface elevation [26]. ARIMA modeling is a method for predicting a value based on its past and present values and is obtained by combining the autocorrelation method with order p with the moving average method with order q and is calculated according to Eq. (7) [26,31].

$$y_t=\sum_{i=1}^{p}u_i y_{t-i}+\sum_{i=1}^{q}u_i\delta_{t-i}+\delta_t \quad (7)$$

where y_t is the observed value at time t, p denotes the autocorrelation component, q is the moving average component, u_i is autocorrelation coefficients, δ_t is the error value at time t and δ_{t-i} is the error value at time $t-i$. The value of δ_t is calculated according to Eq. (8) [26,31].

$$\delta_t=y_t-y_t' \quad (8)$$

Where y_t' represents the predicted value at time t. Prediction of water surface elevation using the ARIMA model increases the efficiency by reducing the beam orientation time for faster waves.

To enable real-time beam steering, data from 12 ultrasonic sensors (operating at different frequencies) is continuously collected and updated. For each sensor $S_{j,i}: j\in\left[1,12\right]\wedge i\in\left[1,n\right]$, with $n\in\left[50,100\right]$, the last n samples are stored during the full wave sampling period (e.g., 5

seconds). Each sensor's data is modeled as a time series; if non-stationary, it is stabilized via $L-times$ differencing. ARIMA modeling is then applied by estimating the autoregressive order p, moving average order q, and autocorrelation coefficients u_i using autocorrelation function (ACF), partial autocorrelation function (PACF), and maximum likelihood. After training and validation, predictions from all sensors are averaged to estimate wave elevation and optimally time laser transmission. The results, compared to actual measurements (see Section 3.4.1), confirm the ARIMA model's accuracy.

3.5. Reconstruction of the shape of the water surface

At this stage, the samples taken by the array of 12 ultrasonic sensors are reconstructed to produce a continuous water surface for each frame, so that the water elevation can be determined at different points. In recovering the sensed data, according to Eq. (9) [17,18], we use norm 1 to minimize the samples taken and find the sparsest solutions applicable to all the measurements.

$$Min\|X\|_1 \; S.T\; Y\begin{bmatrix} y_1 \\ \vdots \\ y_M \end{bmatrix}_{M\times 1} = \Psi\begin{bmatrix} \psi_{11} & \cdots & \psi_{1N} \\ \vdots & \ddots & \vdots \\ \psi_{M1} & \cdots & \psi_{MN} \end{bmatrix}_{M\times N} \times X\begin{bmatrix} X_1 \\ \vdots \\ X_N \end{bmatrix}_{N\times 1} : M > 2SX\log_{10}^{\frac{N}{SX}} \qquad (9)$$

Here, if the number of samples (N) is more than that of measurements (M), we will have an infinite number of answers. Therefore, taking sparsity into account, we can choose the sparsest answer and optimally perform data recovery.

3.6. Calculation of the incidence point

In this section, utilizing the data obtained from the water surface reconstruction phase, we calculate the optimal light beam incidence point on the water surface (wave) to optimize the path of the refracted light toward the receiver. As illustrated in Fig. 6, for each possible point on the water surface (wave), we can determine the direction vector of the refracted light according to Snell's law and the direction vector from the incidence point to the receiver. Subsequently, employing the gradient ascent algorithm, we compute the optimal incidence point of the light beam on the water surface.

In Fig. 6, p represents the Snell parameter, $\left(x, y, h\left(x, y\right)\right)$ denotes the coordinates of the incident light's point of intersection with the water surface, $\vec{r}$ is the direction vector of the

refracted light, $\vec{t}$ represents the direction vector from the point of intersection to the receiver, $\vec{n}$ is the unit normal vector of the surface at the point of intersection, and α is the angle between the incident light direction vector and the surface unit normal vector. Here, we seek to find the point of intersection that minimizes the angle between $\vec{r}$ and $\vec{t}$; therefore, our objective function is defined according to Eq. (10). In this context, the goal is to maximize $\mathrm{Cos}\,\theta$.

$$\mathrm{Cos}\,\theta = \frac{\left[\left(x_r \times x_t\right) + \left(y_r \times y_t\right)\right]}{\left(\left[\frac{\partial h}{\partial x'}\frac{\partial h}{\partial y'} - 1\right] + \left[\left(\frac{\mathrm{Sin}\,\beta}{\mathrm{Sin}\left(\alpha - \beta\right)}\right) \times \left(\vec{m}\right)\right]\right) \times \left(\left|\vec{t}\right|\right)} \tag{10}$$

In this equation, θ represents the angle between $\vec{r}$ and $\vec{t}$; x_r and y_r are the components of the unit vector $\vec{r}$; x_t and y_t are the components of the unit vector $\vec{t}$; $\left|\vec{t}\right|$ denotes the magnitude of $\vec{t}$; $\vec{m}$ is the incident light direction vector; $\left(\frac{\partial h}{\partial x}, \frac{\partial h}{\partial y}, -1\right)$ represents the surface unit normal vector at the point where the incident light intersects the water surface (this vector is derived from the partial derivatives of Eq. (1) with respect to x and y at the point of intersection, $\left(x, y, h\left(x, y\right)\right)$; β represents the angle between $\vec{r}$ and $\vec{n}$; $\alpha - \beta$ is the angle between $\vec{r}$ and $\vec{m}$; and $\frac{\mathrm{Sin}\,\beta}{\mathrm{Sin}\left(\alpha - \beta\right)}$ denotes the Snell parameter, which has been calculated according to Snell's law and the law of sines. Fig. 7 illustrates the optimization flowchart implemented using the gradient ascent method.

In the optimization process, for each new frame obtained from the data measured by the ultrasonic sensors, the optimal path of the beam entering the water is determined. To do so, in each repetition of the gradient ascent algorithm, first, the gradient of the target function ($\mathrm{Cos}\,\theta$) is calculated concerningis calculated relative θ. Then, using the chain law, the gradient of θ to the coordinates of the light-incidence point on the water surface, and finally, the gradient of the target function is obtained concerning the coordinates of the light-incidence point on the water surface. This work contributes to the step-by-step calculation of the gradients and considers the relationship between the dependent variables. Therefore, it is necessary to use the chain law here to calculate the gradient of the target function concerning the main optimization

variable, i.e., the coordinates of the light-incidence point on the water surface. As shown in Fig. 7, in determining the optimal path of light entering water using the incremental gradient algorithm, we consider the learning rate ($\tilde{n}$) as 0.01. This rate is determined in such a way that a proper balance is created between accurate learning from the training data and new data, preventing overfitting occurrence. At first, we consider an initial point ($P_{Initial}$) called the initial incidence point on the water surface, then we try to find an optimal next point (P_{Next}) using the algorithm. Pnext is a new value of the initial incidence point ($P_{Initial}$), obtained by adding a small amount of the learning rate ($\tilde{n}$). The inherent spatial and temporal continuity of water waves, coupled with the findings of optimization analysis, suggests that the new incidence point should be proximate to its predecessor due to the minimal deformation of the water surface between consecutive frames. Consequently, in this approach, we initialize the incidence point for each frame with the incidence point of the preceding frame. The process of adding a small amount of learning rate to the initial incidence point is repeated until the initial collision point value is changed to an optimal value. Here, at each step, the incidence point value moves in the direction of the gradient. In addition, we consider the accuracy tolerance (ε) to be 0.005 to ensure sufficient accuracy in performing calculations, making them close to reality. If the calculation accuracy (e) is less than the accuracy tolerance (ε), the target is met and the algorithm is stopped. Finally, after calculating the optimal incidence point (determining the value of P_F), we calculate the angle of entry of the beam irradiated into the water at this point (α) according to Fig. 8.

For this purpose, since our primary focus is on the water surface and its shape at a specific moment, we can consider the surface function, with the aim of reducing problem dimensions and simplifying it, according to the model described in section 2.2 and without considering temporal variations, as shown in Eq. (11)..

$$y = f(x) \tag{11}$$

By calculating the first derivative of the surface function (Eq. (11)) at the incidence point (P_F), the tangency point of the water surface can be calculated. Therefore, the slope of the line at the incidence point P_F is calculated according to the Eq. (12).

$$m_{PQ} = f'\left(x_{P_F}\right) \tag{12}$$

On the other hand, to calculate the hitting angle of the irradiated beam and water (α), we need to calculate the slope of the line SP_F and the slope of the line MN. Here we can determine the slope of the SP_F line according to the Eq. (13).

$$m_{SP_F} = \frac{y_S - y_{P_F}}{x_S - x_{P_F}} = \frac{y_S - f(x_{P_F})}{x_S - x_{P_F}} \quad (13)$$

Besides, since the two lines MN and PQ are perpendicular to each other, the slope of the MN line can be calculated considering Eq. (12) according to Eq. (14) as follows.

$$m_{MN} = \frac{-1}{m_{pq}} = \frac{-1}{f'(x_{P_F})} \quad (14)$$

Here, the incidence angle of the irradiated beam and water (α) is calculated according to Eq. (15).

$$\alpha = \text{Arctan}\left(\frac{m_{SP_F} - m_{MN}}{1-(m_{SE} \times m_{MN})}\right) \quad (15)$$

In the calculations carried out here, it is assumed that the transmitter is in the air and the receiver is in the water, but if the places of the transmitter and the receiver are changed, we can oppositely solve the problem.

3.7. Stegnagraphy of communication and secure and lightweight data transmission

At this stage, after simultaneous compression and encryption of the data, according to the process described in steps 3-2, using a stealth modulator on the Amplified Spontaneous Emission (ASE) noise inherent in the optical channel, they become modulated and hidden. Then, in the next step, the stealth signal obtained using a Chirped Fiber Bragg Grating (CFBG) is dispersed in time and transmitted in the channel. In this technique, by reducing the power of the data carrier signal, the transmitted from the ASE noise data becomes indistinguishable. In this process, the security is dependent on CFBG parameters and the receiver needs to access these parameters to recover the signal containing data. The process steps are shown in Fig. 9.

3.8. Receiving stealth signal, dispersion in time, and decryption and extraction of original data

At this stage, after receiving the stealth signal by the air nodes network, the stealth signal is compressed in time by the compressor and separated from the ASE noise using a Stealth Demodulator. In the following, using a decryptor unit, the data is simultaneously decompressed

and used by the air nodes network in the form of original data. In Fig. 10, the described steps are shown.

4. **Setting of simulation parameters**

To ensure consistency, both the proposed and SDVLN methods [27] were simulated under identical conditions using MATLAB R2024b and Zemax 2024 on a high-performance system. Nodes were randomly placed in dynamic air and water environments, with variable spatial positions and water surface levels influenced by environmental factors. The air-water link length was computed based on actual node positions and dynamic surface variations. It should be noted that the simulation parameters were set according to Table 2.

5. **Analysis and evaluation of the results**

In this section, we present the performance and security evaluation results of the proposed protocol compared to the SDVLN method [27]. The evaluation was conducted through computer simulations and mathematical calculations, considering metrics such as signal strength, transmission capacity, energy consumption, and signal-to-noise ratio of the recovered signal.

5.1. Signal power analysis and evaluation

In this section, we employ signal strength as a metric to evaluate communication quality. Eq. (16) [29] expresses how the received signal power is calculated based on variations in the divergence angle and line-of-sight distance between transmitter and receiver.

$$P_{al} = \frac{P_{ve}\eta_a l \eta_{ve} \exp\left[\frac{-\left(\alpha(\lambda)+\beta(\lambda)\right)d}{\mathrm{Cos}\,\theta}\right] D^2 \mathrm{Cos}\,\theta}{8d^2\left(1-\mathrm{Cos}\,\theta_0\right)} \tag{16}$$

In this equation, P_{al} is the power of the optical signal received by the receiver in dBm, P_{ve} represents the transmitter's optical power in watts, η_{al} denotes the optical efficiencies of receiver, η_{ve}, indicates the optical efficiencies of transmitter, θ is the angle between the perpendicular to the receiver plane and the transmitter-receiver projection in degrees, θ_0 represents the beam divergence angle in degrees, D is the receiver's diaphragm diameter in centimetres, d denotes the line-of-sight distance between the receiver and the transmitter

planes, $\alpha(\lambda)$ and $\beta(\lambda)$ represent the absorption coefficient and scattering coefficient of pure seawater at wavelength λ, respectively.

Fig. 11 (a) compares received signal strength versus beam divergence angle for the proposed protocol and SDVLN method [27], using a 10 m link and a 50 cm receiver diaphragm.

As illustrated in Fig. 11 (a), increasing the beam divergence angle reduces received signal strength due to defocusing, but this reduction is significantly lower using the proposed protocol compared to SDVLN [27] (28.16% less at $15°$ and 22.49% less at $45°$). Fig. 11 (b) shows that as the line-of-sight distance increases (at $5°$ divergence and 50 cm receiver aperture), photon scattering causes signal attenuation; however, the proposed method mitigates this effect, reducing degradation by 18.29% at 20 meters versus SDVLN [27]. The gentler slope in both figures confirms greater robustness and signal stability of the proposed approach under increasing divergence angles and distances, indicating superior performance and reliability.

5.2. Analysis and evaluation of transmission channel capacity

Channel capacity in a light-based communication system can be defined as the maximum error-free information transmission rate [28]. Here, channel capacity is a function of various factors, including the type and atmospheric conditions of the propagation environment, as well as parameters such as laser wavelength and power, modulation type, detector characteristics, distance and alignment between transmitter and receiver, and receiver diaphragm diameter [29]. In this research, in addition to the received signal power criterion, channel capacity has been employed as a key metric to evaluate the performance of the proposed protocol in comparison with the SDVLN method [27]. In the simulation, this metric was calculated based on Eq. (17) [29].

$$C=\frac{1}{2}B\log_2\left(1+\frac{P_{ve}\eta_a l\eta_{ve}\exp\left[\frac{-(\alpha(\lambda)+\beta(\lambda))d}{\cos\theta}\right]D^2\cos\theta}{\left(\frac{2qS\pi^2D^2(FOV)^2\Delta\lambda T_F ERL_{fac}e^{(-kh)}B}{4\pi}+2qI_DB+\frac{4K_BT_KFB}{R_L}\right)8d^2(1-\cos\theta_0)}\right) \quad (17)$$

In this equation, C represents the channel capacity in bits per second, B is the electrical bandwidth of the photodetector in Hertz, q is the elementary charge in Coulombs, S is the sensitivity of the photodetector in amperes per watt, FOV is the field of view of the system in degrees, $\Delta\lambda$ is the bandwidth of the optical filter, T_F is the optical filter transmissivity, E is

the downwelling irradiance, R is the underwater reflectance of the downwelling, L_{fac} is the factor that describes the directional dependence of the underwater radiance, K is the attenuation coefficient, h is the depth of the receiver, I_D is the dark current in nanoamperes, K_B is the Boltzmann constant, T_K is the temperature in Kelvin, F is the noise figure of the system, and R_L is the load resistance of the photodetector in ohms.

Fig. 12 (a) shows that increasing the divergence angle reduces channel capacity exponentially due to optical signal defocusing. At a 10 m distance in pure seawater, a 1° to 30° divergence increase leads to a 55.67% capacity drop. Nonetheless, the proposed method outperforms the SDVLN method [27] by 5.57%, thanks to its optimized optical design and content-aware sampling.

As depicted in Fig. 12 (b), increasing the receiver diaphragm diameter significantly boosts channel capacity. At a 10 m distance and 5° beam divergence, a 50-fold diaphragm increase yields a 4-fold capacity gain, enabling a 370 Mbps transmission rate due to enhanced photon reception.

As shown in Fig. 12 (c), increasing the transmitter-receiver distance reduces channel capacity due to greater photon scattering and attenuation. With a 5° divergence angle and 50 cm receiver diaphragm, the proposed model consistently outperforms the SDVLN method [27] across varying distances.

5.3. The amount of used energy

Energy consumption serves as another crucial metric for assessing the proposed communication model's efficiency in this study. To compare the efficiency of our proposed communication model to the SDVLN method [27], we calculate energy consumption using Eq. (18) [18].

$$E_{Usage} = E_{Usage-Sensing} + E_{Usage-Communication} \quad (18)$$

In this equation, E_{Usage} represents the energy consumption of the communication model, $E_{Usage-Sensing}$ represents the energy expended for data sensing, and $E_{Usage-Communication}$ represents the energy expended for transmitting the sensed data. Here, the energy utilized for data sensing comprises the energy expended for original data acquisition, the energy used for compressing

and securing the acquired data, and the energy consumed for background processing. Its calculation is determined by Eq. (19) [18].

$$\begin{aligned} E_{Usage-Sensing} &= \left[N \times P_{Acquisition} \times T_{Instruction-Execution} \right] \\ &+ \left[NE_{Mrd} + MNE_{Mul} + \left(MN - N \right) E_{Add} + ME_{Mwr} \right] \\ &+ \left[P_{Background} \times \left[N + MN + \left(MN - N \right) + M \right] \right] \\ &\times \left[T_{Instruction-Execution} \right] \end{aligned} \tag{19}$$

This equation incorporates several key parameters to represent energy consumption. N signifies the number of samples involved. $P_{Acquisition}$ represents the total power consumed for data sensing, encompassing both the processor and sensor circuit power consumption. $T_{Instruction-Execution}$ represents the time required to execute a single instruction. E_{Mrd} signifies the energy required to read a single bit of data from memory. M denotes the total number of measurements performed. E_{Mul} represents the energy consumed during a multiplication operation. E_{Add} signifies the energy consumed during an addition operation. E_{Mwr} represents the energy required to write a single bit of data to memory. Finally, $P_{Background}$ represents the power consumed by the processor when inactive. Additionally, the energy consumption associated with transmitting the sensed data is calculated using Eq. (20) [18].

$$E_{Usage-Communication} = \frac{T_{Transmit} \times E_{Pulse} \times M}{PW} \tag{20}$$

In this equation, three key parameters are denoted by $T_{Transmit}$, E_{Pulse} , and PW . $T_{Transmit}$ represents the time in seconds required to transmit a single bit of data. E_{Pulse} represents the pulse energy measured in Joules, and PW represents the pulse width in seconds. Fig. 13 illustrates a performance analysis of the proposed communication model's energy consumption. This analysis considers a communication distance of 1 meter, a pure seawater environment, and a 2-millisecond activity interval. It also examines the effect of varying entropy levels with dynamic compression rates that adjust according to the degree of sparsity and entropy in the sensed data. The performance of our proposed model is compared to the SDVLN method introduced earlier [27].

As depicted in Fig. 13, the proposed model reduces energy consumption compared to the SDVLN method [27], with a 7.63% improvement at an entropy level of 0.9150 Bits. This gain

is more pronounced at lower entropy levels, where the model operates in more steps. By leveraging entropy-aware sampling and adaptive compression based on data sparsity, the proposed model transmits fewer bits than SDVLN [27] for the same sensed data, resulting in lower transmitter energy consumption.

5.4. Security Analysis and Evaluation of the Communication protocol

In the present section, we investigate the security of the communication model against an intruder who tries to recover the stealth signal by guessing the ASE noise bandwidth parameter and CFBG scattering parameter. In this scenario, we presume that the intruder possesses the requisite analog signal processing tools, including a tunable bandwidth selector to identify the ASE noise bandwidth and a tunable dispersion compensator to compress the stealth signal. In line with Kerckhoffs's principle, a system's security hinges entirely on the secrecy of its key. As long as the encryption key remains confidential, even if an intruder gains access to the encryption scheme's details, they cannot decrypt the protected information.

In the proposed communication model, the system parameters used for implementation create a very large set of possible combinations of keys. These combinations are so many that they are practically considered semi-infinite. Here, the intruder needs to match its own ASE noise bandwidth ($\Delta v_{Intruder}$) and CFBG dispersion parameter of its device ($D_{Intruder}$) to the values used on the signal-masking transmitter side to disperse the stealth data, which is difficult. Here, if the bandwidth chosen by the intruder ($\Delta v_{Intruder}$) is too narrow, its overlap with the correct ASE noise bandwidth ($\Delta v_{Overlap}$) is not large enough to help signal recovery, but if this bandwidth is chosen too high, although the chance of overlapping is higher, a lot of additional noise will enter the recovered signal. Therefore, to check the usability of the stealth signal recovered by the intruder, using Eq. (21) [32], the SNR ratio of the signal recovered by the intruder ($SNR_{Intruder}$), to the SNR of the signal recovered by the Legitimate Receiver (SNR_{Main}), is quantified.

$$\frac{SNR_{Intruder}}{SNR_{Main}} = \frac{\Delta v^2 Overlap\left(Z_1 + Z_2 \Delta v_{CFBG}\right) DRR}{\Delta v^2{}_{CFBG}\left(Z_1 + Z_2 \Delta v_{Intruder}\right)}$$
$$Z_1 = \frac{4K_B T_K F_n B}{R_L} \; and \; Z_2 = 4R^2 S_{sp}^2 B + 4qRS_{sp} B \tag{21}$$

where Δv_{CFBG} is the bandwidth of the correct ASE noise carrying stealth data, S_{sp} is the

spectral density of the ASE noise, B denotes the electric bandwidth of photodetector in amps per watt, F_n represents the amplification ratio of the electric amplifier in the photodetector, q is electron charge in coulombs, R is responsivity of the photodetector, R_L, denotes load resistance of the photodetector, T_K is the temperature in kelvin, and DDR is dispersion recovery ratio whose value is calculated considering the intruder dispersion ($DIntruder$) and the correct dispersion of the CFBG (DCFBG) parameters according to the Eq. (22) [32].

$$DDR=\begin{cases}\dfrac{\sqrt{1+\left(D_{Intruder}\Delta\lambda_{Overlap}e_{Intensity}\right)^2}}{\sqrt{1+\left(D_{CFBG}\Delta\lambda_{CFBG}e_{Intensity}\right)^2}} & When\ D_{Intruder}<D_{CFBG}\\ \dfrac{\sqrt{1+\left[\left(2D_{CFBG}-D_{Intruder}\right)\Delta\lambda_{Overlap}e_{Intensity}\right]^2}}{\sqrt{1+\left(D_{CFBG}\Delta\lambda_{CFBG}e_{Intensity}\right)^2}} & When\ D_{CFBG}<D_{Intruder}<2D_{CFBG}\\ \dfrac{1}{\sqrt{1+\left[\left(-D_{CFBG}+D_{Intruder}\right)\Delta\lambda_{CFBG}e_{Intensity}\right]^2}} & When\ D_{Intruder}>2D_{CFBG}\end{cases} \quad (22)$$

Here, the result of the investigation shows that the overall success rate of the intruder for the simultaneous effective matching of the two parameters of ASE noise bandwidth and CFBG dispersion is about 2^{-10}. Therefore, given the fact that data is generally transmitted at a high rate over the channel, the intruder must recover the stealth signal exactly at the moment of receiving it. Since the intruder lacks prior knowledge, they have only a single attempt to guess the system parameters used to generate the real-time stealth signal. Even attempting a search algorithm to identify these parameters would be time-consuming, especially if the intruder relies on physical hardware. This vulnerability can be effectively mitigated by employing standard cryptographic pseudorandom number generators (CSPRNGs) and a pre-shared secret key. This approach ensures that the system parameters are updated for each transmitted data bit, rendering them unpredictable and significantly more difficult for an intruder to crack.

6. **Conclusion and future work**

In this research, we aimed to develop a secure and energy-efficient covert communication protocol focusing on multi-domain (air-water) communication challenges. The proposed protocol establishes a reliable connection between nodes deployed in both aquatic and aerial environments, while providing bidirectional and direct communication capabilities with

favorable transmission range and data capacity. To achieve this, our proposed model employs an entropy-based data sampling approach, followed by simultaneous compression and encryption tailored to the data's sparsity. Subsequently, we concealed the resulting output by modulating it onto ASE noise, and finally dispersed it in time using a chirped fiber bragg grating (CFBG) and transmitted it through an optical wireless communication link.

In the proposed protocol, we employed an array of ultrasonic sensors coupled with an ARIMA model for predicting water surface dynamics to adapt the communication link to water dynamics, enabling surface scanning, profile reconstruction, and optimal impact point determination. Here, we utilized an optimized optical system for target detection and light beam steering across an extensive 174-degree range. Furthermore, by implementing OOK pulse-based modulation alongside laser diode switching, we significantly enhanced the data transmission rate while substantially reducing energy consumption.

In this research, we evaluated the performance and security of the proposed communication protocol based on specific metrics including received signal strength, channel capacity, energy consumption, and recovered signal-to-noise ratio, using computer simulations and mathematical calculations in comparison with the SDVLN method [27]. We demonstrated how the proposed protocol can enhance security, transmission capacity, and received signal strength while reducing energy consumption. In this study, we conducted simulations at various entropy levels and for different numbers of measurements. It is evident that as the number of measurements increases and approaches the total number of samples, the reconstruction quality improves while simultaneously enhancing security and making unauthorized data recovery infeasible.

Here, this increase in quality, in the phase of reconstructing the shape of the water surface, will play a key role in increasing the accuracy of orienting the laser beam, causing the energy consumption to decrease while maintaining the reliability and bandwidth of the communication link. On the other hand, due to the increase of entropy by affecting the amount of information content and compression rate in the sampling phase, sensed data in the communication model with the same size as the sensed data in the SDVLN method [27] is transmitted with the lower number of bits and energy consumption compared to the SDVLN method [27].

However, the proposed communication protocol, despite outperforming the benchmark SDVLN [27] method, incurs higher implementation and computational costs. Consequently, in

future research, we intend to replace the current ultrasonic sensor array and optical system with a UV-A laser-based adaptive optical system, which will maintain data exchange capabilities while enabling various additional functionalities. These functionalities include detection, tracking, and reconstruction of the water surface profile, as well as optimal impact point determination, all of which will be integrated and implemented within the same system. This replacement will not only reduce implementation costs but also decrease the computational overhead.

7. Acknowledgment

This research was financially supported by the University of Mazandaran under research grant No. 20/33662 as part of a postdoctoral project.

References

[1] Spencer, D. K., Duncan, S., Taliaferro, A., "Operationalizing artificial intelligence for multi-domain operations: a first look," in Artificial Intelligence and Machine Learning for Multi-Domain Operations Applications, 2019, p. 1100602. DOI: https://doi.org/10.1117/12.2524227

[2] Aman, W., Al-Kuwari, S., Kumar, A., et al., "Underwater and air-water wireless communication: state-of-the-art, channel characteristics, security, and open problems," arXiv preprint arXiv:2203.02667, 2022. DOI: https://doi.org/10.48550/arXiv.2203.02667

[3] Cui, J.-H., Kong, J., Gerla, M., et al., "The challenges of building mobile underwater wireless networks for aquatic applications," IEEE Network, vol. 20, pp. 12-18, 2006. DOI: https://doi.org/10.1109/MNET.2006.1637927

[4] Shantaram, A., Beyenal, H., Veluchamy, R., et al., "The challenges of building scalable mobile underwater wireless sensor networks for aquatic applications," Environ. Sci. Technol., vol. 39, pp. 5037-5042, 2005. DOI: https://doi.org/10.1021/es0480668

[5] Aman, W., Al-Kuwari, S., Muzzammil, M., et al., "Security of underwater and air–water wireless communication: state-of-the-art, challenges and outlook," Ad Hoc Networks, vol. 142, p. 103114, 2023. DOI: https://doi.org/10.1016/j.adhoc.2023.103114

[6] Qu, F., Qian, J., Wang, J., et al., "Cross-medium communication combining acoustic wave and millimeter wave: theoretical channel model and experiments," IEEE Journal of Oceanic Engineering, vol. 47, pp. 483-492, 2021. DOI: https://doi.org/10.1109/JOE.2021.3120373

[7] Mohammed, A. S., Adnan, S. A., Ali, M. A. A., et al., "Underwater wireless optical communications links: perspectives, challenges and recent trends," Journal of Optical Communications, vol. 45, pp. 937-945, 2024. DOI: https://doi.org/10.1515/joc-2022-0063

[8] Esmaeili, S., Ghasemi, J., "A location-aware covert communication protocol in inter-environmental communication applications," Alexandria Engineering Journal, vol. 123, pp. 592-609, 2025. DOI: https://doi.org/10.1016/j.aej.2025.03.087

[9] Carver, C. J., Tian, Z., Zhang, H., et al., "Amphilight: direct air-water communication with laser light," GetMobile: Mobile Computing and Communications, vol. 24, pp. 26-29, 2021. DOI: https://doi.org/10.1145/3447853.3447862

[10] Hu, Q., "Covert Transmission in water-to-air optical wireless communication systems," IEEE Transactions on Information Forensics and Security, 2024. DOI: https://doi.org/10.1109/TIFS.2024.3376965

[11] Peng, J., Tang, S., "Covert communication over VoIP streaming media with dynamic key distribution and authentication," IEEE Transactions on Industrial Electronics, vol. 68, pp. 3619-3628, 2020. DOI: https://doi.org/10.1109/TIE.2020.2979567

[12] Hu, Q., "Covert water-to-air optical wireless communication based on an adversarial autoencoder," IEEE Transactions on Cognitive Communications and Networking, 2025. DOI: https://doi.org/10.1109/TCCN.2024.3524625

[13] Wang, J., "enabling reliable water-air direct optical wireless communication for uncrewed vehicular networks: a deep reinforcement learning approach," IEEE Transactions on Vehicular Technology, 2024. DOI: https://doi.org/10.1109/TVT.2024.3376521

[14] Lin, T., "Real-time water-to-air communication system under dynamic water surface and strong background radiation," IEEE Photonics Journal, 2024. DOI: https://doi.org/10.1109/JPHOT.2024.3407876

[15] Tsai, S.-Y., "Wavy water-to-air optical camera communication system using rolling shutter image sensor and long short term memory neural network," Optics Express, vol. 32, pp. 6814-6822, 2024. DOI: https://doi.org/10.1364/OE.503787

[16] Ghassemlooy, Z., Uysal, M., Khalighi, M. A., et al., "An overview of optical wireless communications," Optical Wireless Communications: An Emerging Technology, pp. 1-23, 2016. DOI: https://doi.org/10.1007/978-3-319-30201-0_1

[17] Esmaeili, S., Tabbakh, S. R. K., Shakeri, H., "A priority-aware lightweight secure sensing model for body area networks with clinical healthcare applications in Internet of Things," Pervasive and Mobile Computing, vol. 69, p. 101265, 2020. DOI: https://doi.org/10.1016/j.pmcj.2020.101265

[18] Esmaeili, S., Shamsi, R., "A lightweight and secure sensing model for body area networks in the Internet of Things in biological warfare applications," Internet of Things, vol. 22, p. 100717, 2023. DOI: https://doi.org/10.1016/j.iot.2023.100717

[19] Massel, S. R., "Surface waves in deep and shallow waters," Oceanologia, vol. 52, pp. 5-52, 2010. DOI: https://doi.org/10.1016/j.iot.2023.100320

[20] Whitman, R. L., Nevers, M. B., Przybyla-Kelly, K., et al., "Physical and biological factors influencing environmental sources of fecal indicator bacteria in surface water," The Fecal Bacteria, pp. 111-134, 2010. DOI: https://doi.org/10.1128/9781555816865.ch6

[21] Masch, F. D., "Cnoidal waves in shallow water," in Coastal Engineering 1964, ed, 1964, pp. 1-22. DOI: https://doi.org/10.1016/j.iot.2023.1001472

[22] Hardy, T. C., Kraus, N. C., "A numerical model for shoaling and refraction of second-order cnoidal waves over an irregular bottom," 1987. DOI: https://doi.org/10.1016/j.iot.2023.1001427

[23] Aionesei, G.-A., Panait, C., "Understanding multi-domain operations from the Air Force perspective," Review of the Air Force Academy, pp. 61-70, 2024. DOI: https://doi.org/10.1016/j.iot.2023.1001215

[24] Schwartz, J. A., "Studies of laser ranging to the TOPEX satellite," in Free-Space Laser Communication Technologies, 1988, pp. 172-179. DOI: https://doi.org/10.1117/12.976562

[25] Gangwar, R. K., Kumar, M., Jaiswal, A., et al., "Performance analysis of image compression using fuzzy logic algorithm," Signal & Image Processing, vol. 5, p. 73, 2014. DOI: https://doi.org/10.1117/12.973517

[26] Yu, Z., Lei, G., Jiang, Z., et al., "ARIMA modelling and forecasting of water level in the middle reach of the Yangtze River," in 2017 4th International Conference on Transportation Information and Safety (ICTIS), 2017, pp. 172-177. DOI: https://doi.org/10.1109/ICTIS.2017.8047762

[27] Enhos, K., Unal, D., Demirors, E., et al., "Breaking through the air-water interface with software-defined visible light networking," IEEE Internet of Things Magazine, vol. 5, pp. 10-16, 2022. DOI: https://doi.org/10.1109/IOTM.001.2200130

[28] Erkmen, B. I., Moision, B. E., Birnbaum, K. M., "A review of the information capacity of single-mode free-space optical communication," Free-Space Laser Communication Technologies XXII, vol. 7587, pp. 191-202, 2010. DOI: https://doi.org/10.1117/12.843542

[29] Mahmutoğlu, Y., Albayrak, C., Türk, K., "Investigation of underwater wireless optical communication channel capacity for different environment and system parameters," Hittite Journal of Science and Engineering, vol. 7, pp. 279-285, 2020. DOI: https://doi.org/10.17350/HJSE19030000197

[30] Dingemans, M. W., "Water wave propagation over uneven bottoms," Advanced Series on Ocean Engineering, 1997. DOI: https://doi.org/10.1142/1241-part2

[31] Adytia, D., "Wind wave prediction by using autoregressive integrated moving average model: case study in Jakarta bay," International Journal on Information and Communication Technology (IJoICT), vol. 4, pp. 33-42, 2018. DOI: https://doi.org/10.21108/IJOICT.2018.42.300

[32] Ma, P. Y., "Steganographic communication via spread optical noise: A link-level eavesdropping resilient system," Journal of Lightwave Technology, vol. 36, pp. 5344-5357, 2018. DOI: https://doi.org/10.1109/JLT.2018.2872422

Figure Captions

Fig. 1 (a). Optical structure of the transmitter's tracking and transmission section.

Fig. 1 (b). The optical structure of the transmitter's detection unit.

Fig. 2. Increasing the direction range of light beams to a total viewing angle of 174°.

Fig 3. Image of a cnoidal wave.

Fig. 4. stages of the proposed covert communication model.

Fig. 5. The placement of the laser diode and ultrasonic sensors in the array.

Fig. 6. Calculation of the incidence point using the gradient ascent algorithm.

Fig. 7. Calculation of the optimal path of light entering the water using the gradient ascent algorithm according to the chain rule.

Fig. 8. The image of the calculation of the incidence angle of the radiated beam and the water surface.

Fig. 9. Secure and lightweight data transmission Communication and encryption process.

Fig. 10. The process of receiving information, decrpting and spreading information.

Fig. 11 (a). The graph of the received signal strength as a function of the divergence angle of the light beam.

Fig. 11 (b). The graph of the received signal strength as a function of distance between the transmitter and the receiver

Fig. 12 (a). Transmission channel capacity diagram versus divergence angle of a light beam variations.

Fig. 12 (b). Transmission channel capacity diagram versus aperture diameter variations.

Fig. 12 (c). Transmission channel capacity diagram versus variations of distance between the transmitter and the receiver.

Fig. 13. Chart of energy consumption in the transmitter component at different levels of entropy and compression rate.

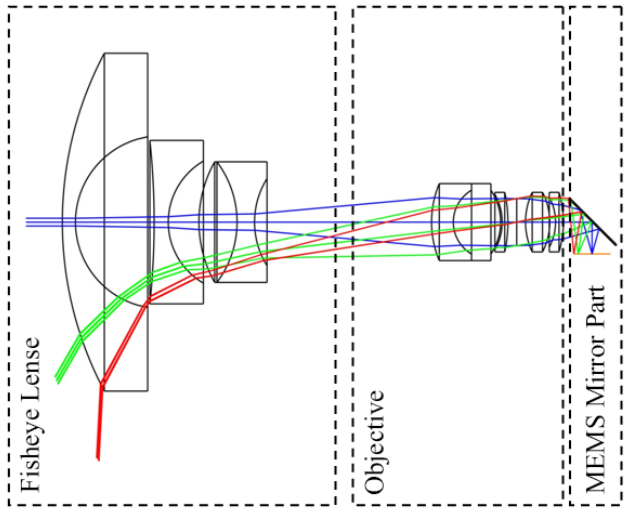

Fig. 1 (a). Optical structure of the transmitter's tracking and transmission section.

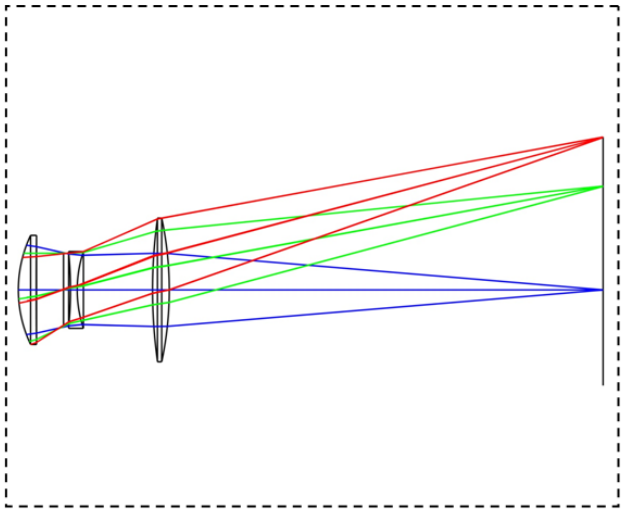

Fig. 1 (b). The optical structure of the transmitter's detection unit.

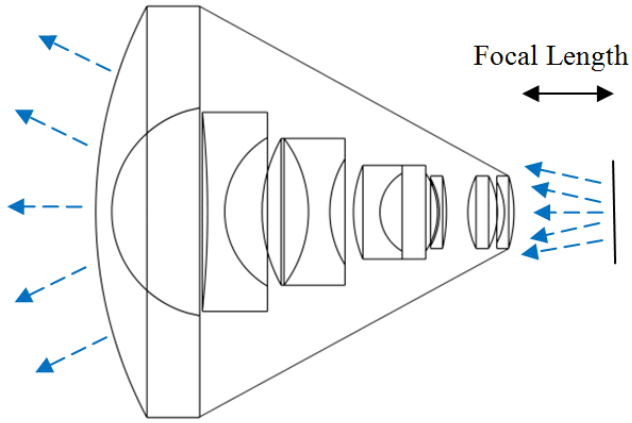

Fig. 2. Increasing the direction range of light beams to a total viewing angle of 174°

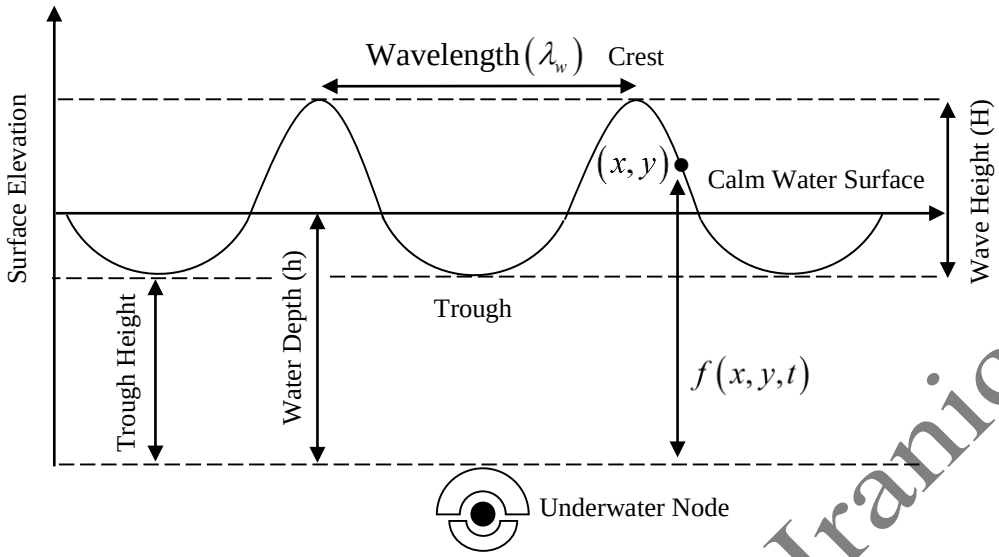

Fig 3. Image of a cnoidal wave

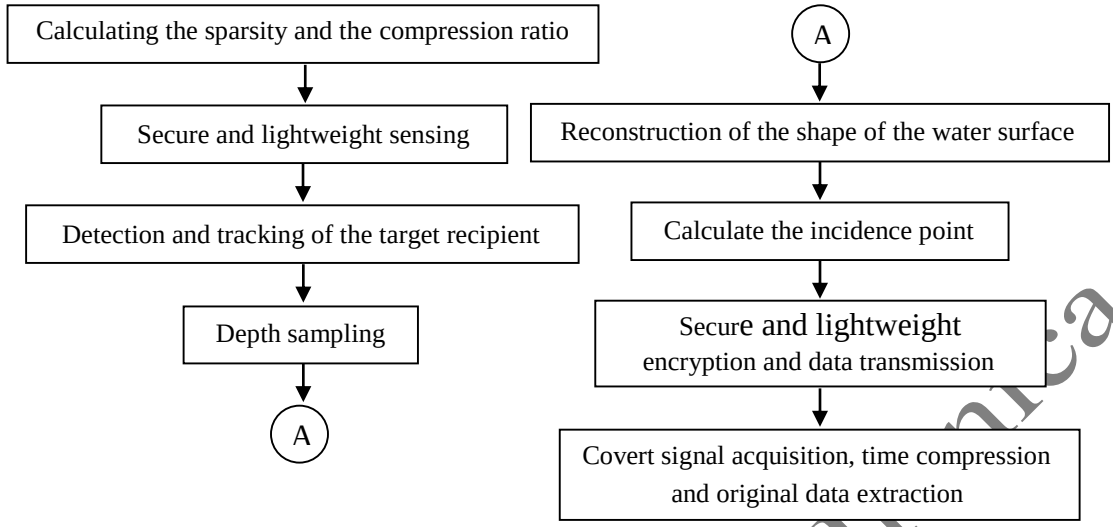

Fig. 4. stages of the proposed covert communication model

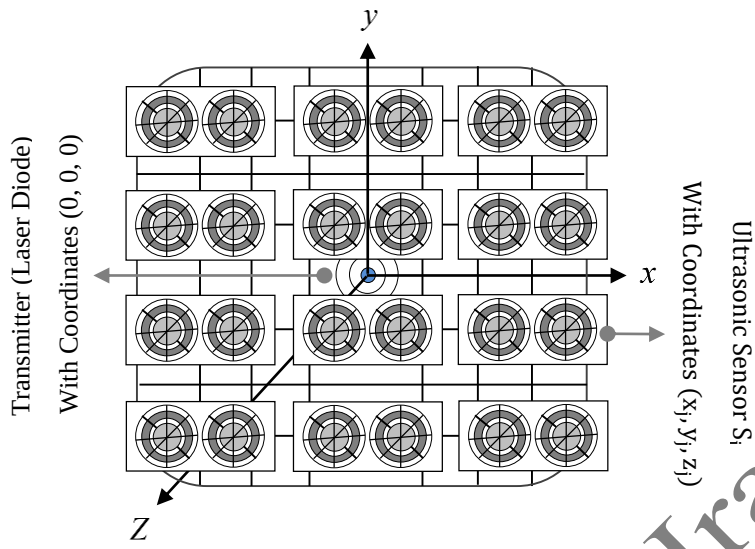

Fig. 5. The placement of the laser diode and ultrasonic sensors in the array

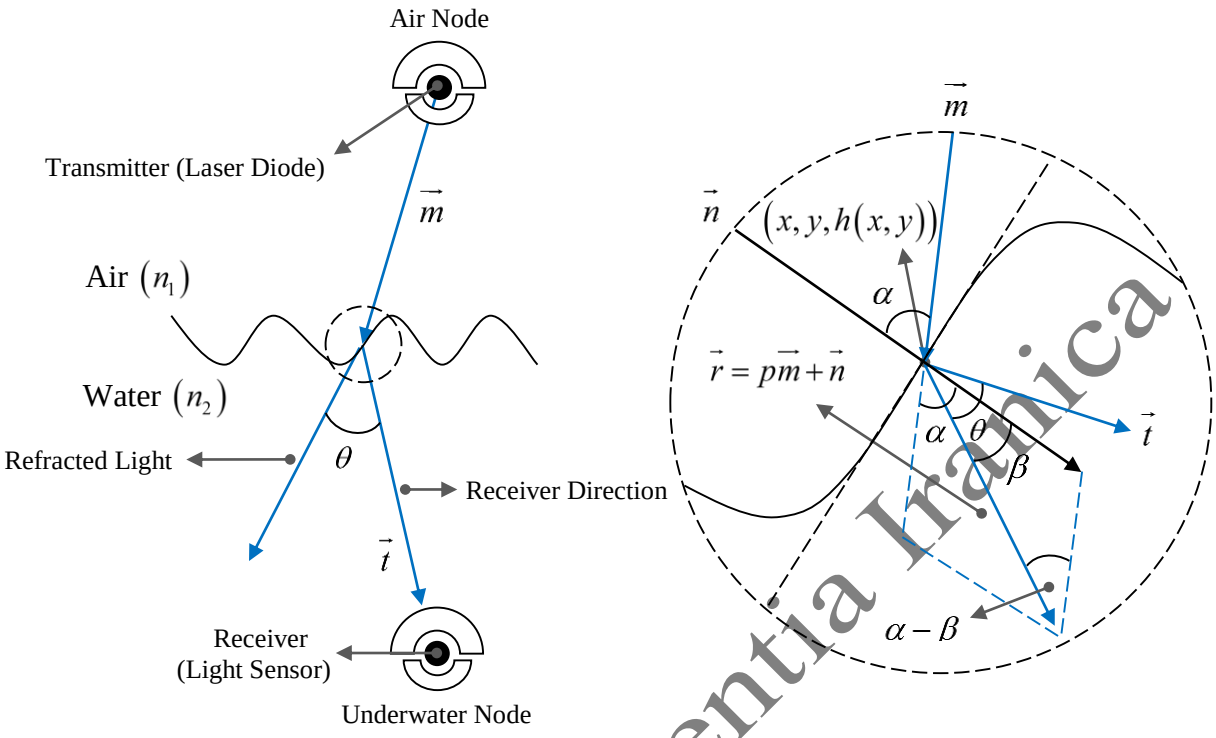

Fig. 6. Calculation of the incidence point using the gradient ascent algorithm.

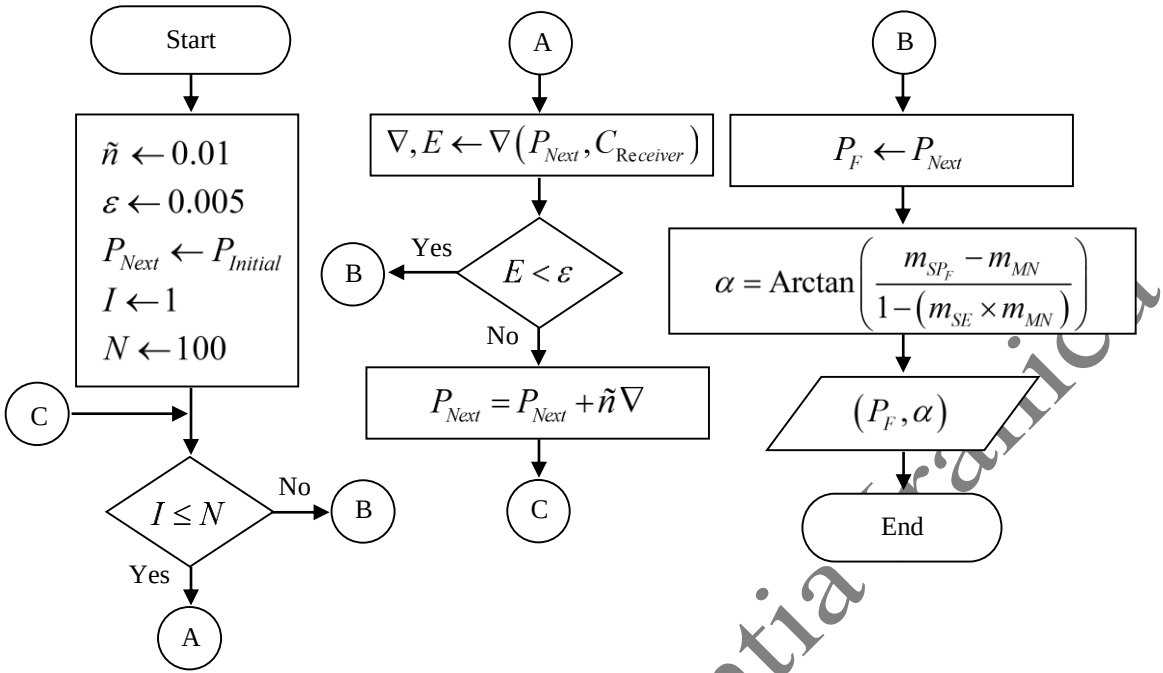

Fig. 7. Calculation of the optimal path of light entering the water using the gradient ascent algorithm according to the chain rule

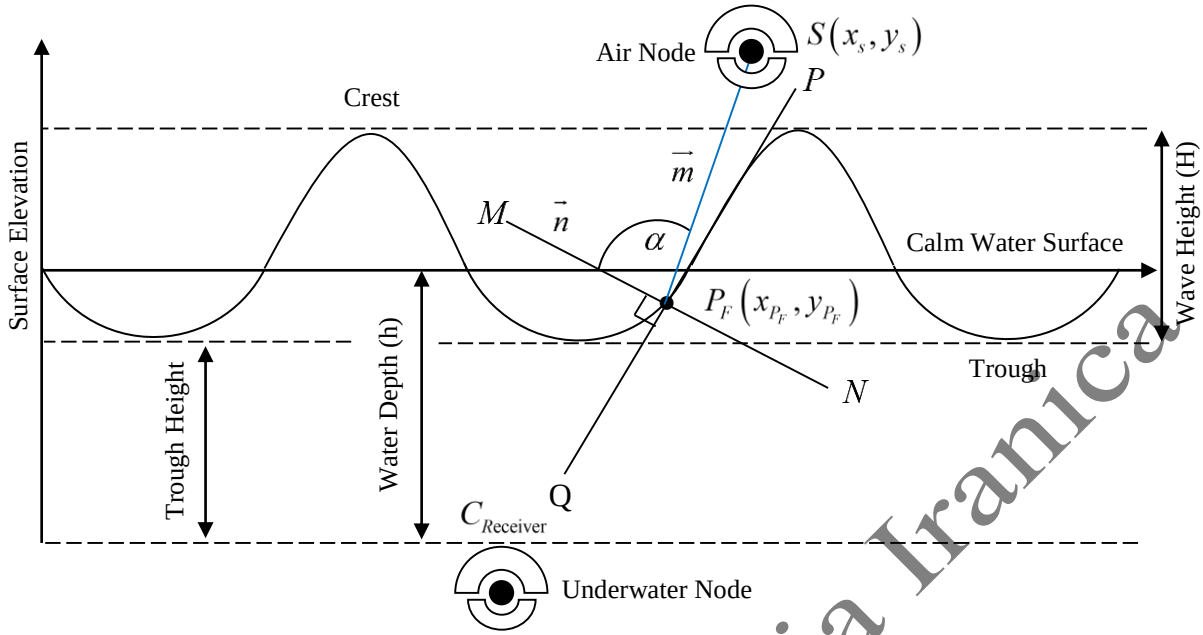

Fig. 8. The image of the calculation of the incidence angle of the radiated beam and the water surface

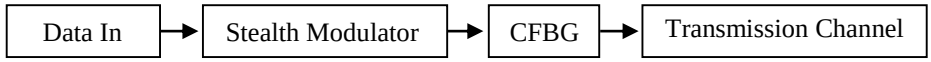

Fig. 9. Secure and lightweight data transmission Communication and encryption process

Fig. 10. The process of receiving information, decrpting and spreading information

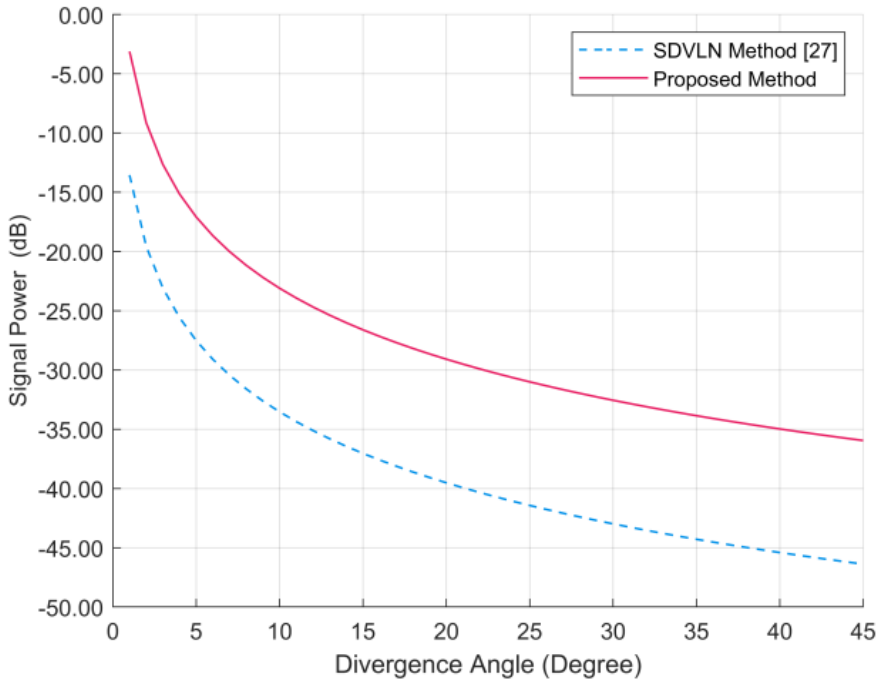

Fig. 11 (a). The graph of the received signal strength as a function of the divergence angle of the light beam

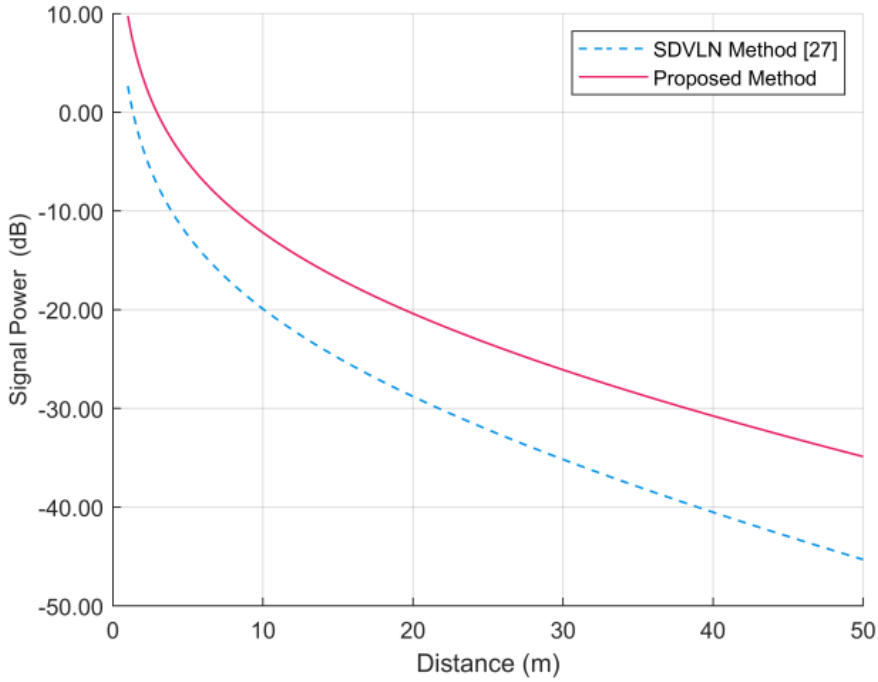

Fig. 11 (b). The graph of the received signal strength as a function of distance between the transmitter and the receiver

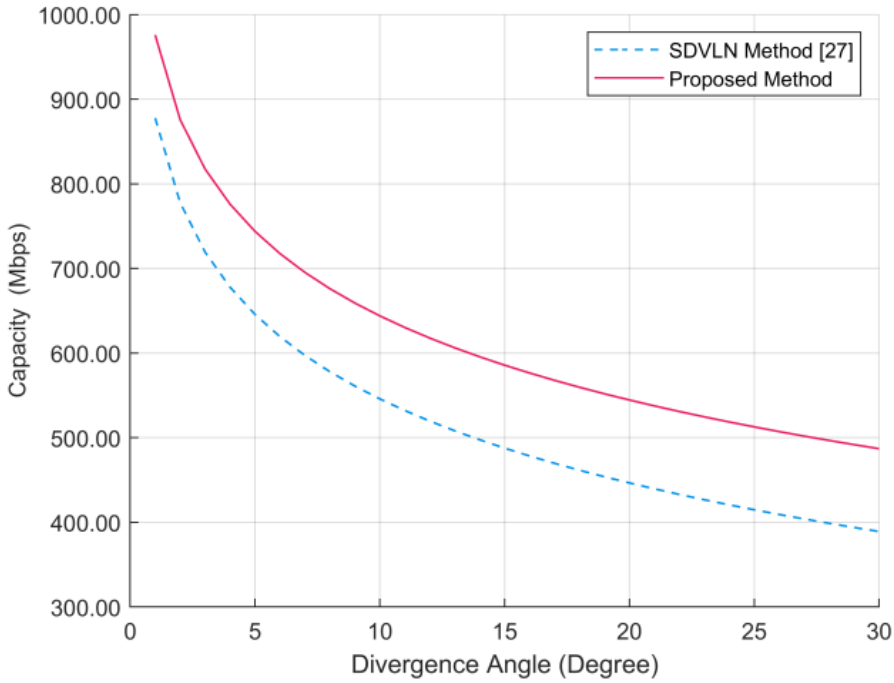

Fig. 12 (a). Transmission channel capacity diagram versus divergence angle of a light beam variations.

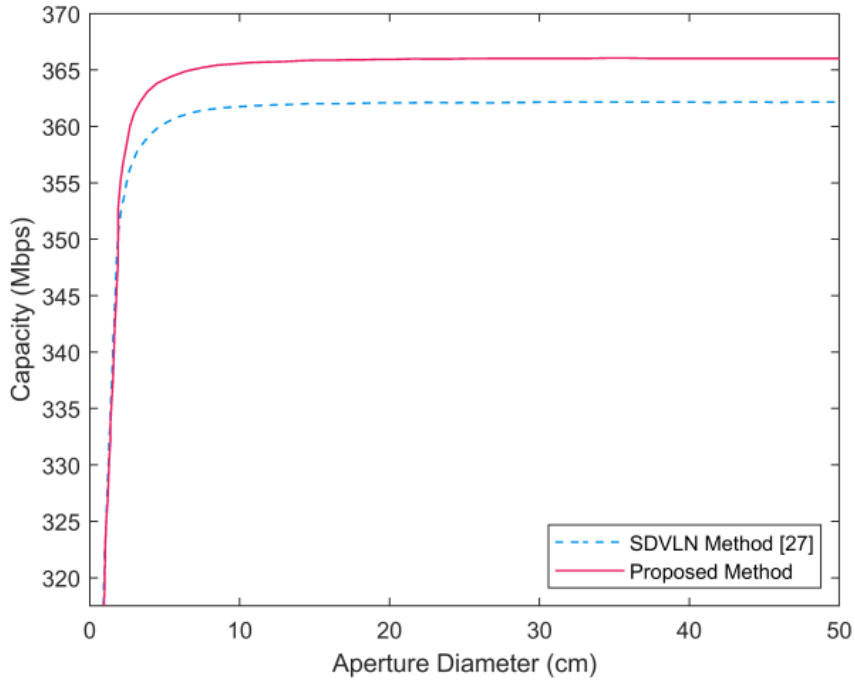

Fig. 12 (b). Transmission channel capacity diagram versus aperture diameter variations.

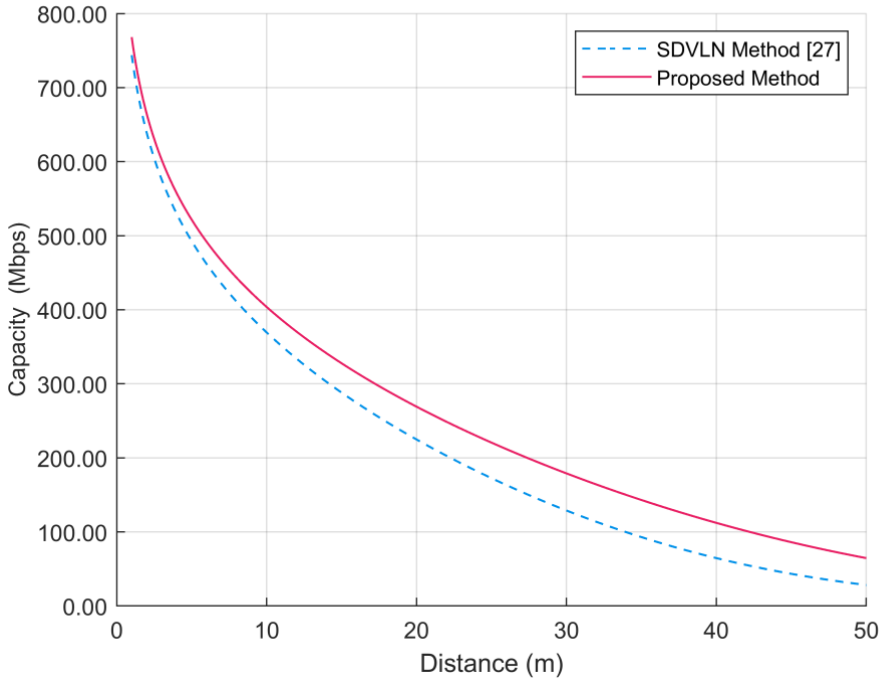

Fig. 12 (c). Transmission channel capacity diagram versus variations of distance between the transmitter and the receiver.

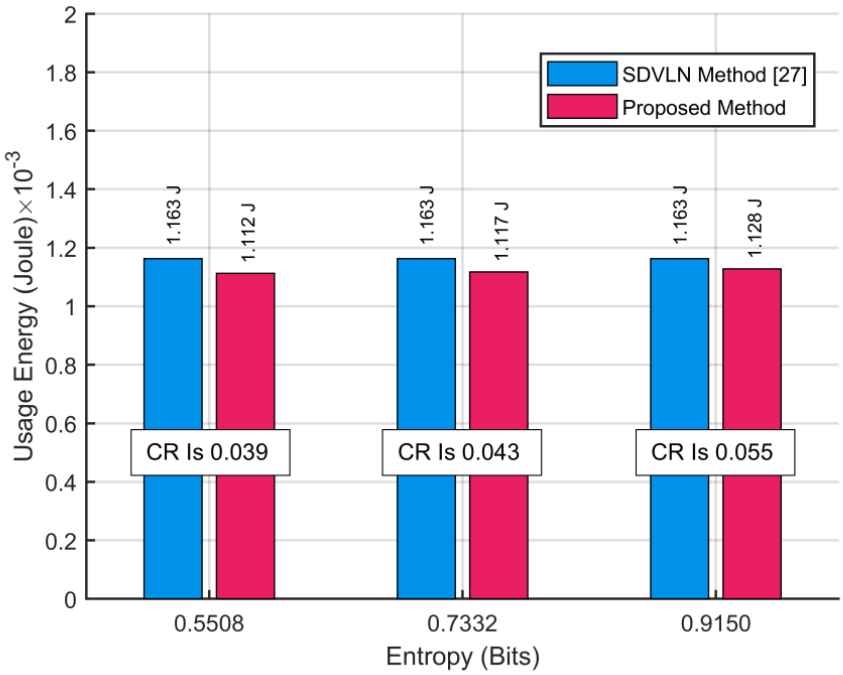

Fig. 13. Chart of energy consumption in the transmitter component at different levels of entropy and compression rate

Table Captions

Table 1. Experiment's Assumptions.
Table 2. Parameter settings in the simulations.

Table 1
Experiment's Assumptions.

No.	Assumption
1.	All data sensed by both underwater and aerial nodes are valid.
2.	Both aerial and underwater nodes are not stationary at a fixed location.
3.	The data acquired from aerial and underwater nodes are sparse in the linear-transform domain.
4.	The measurement follows a linear pattern.
5.	The number of measurements is equal to or more than twice the sparsity level of the sensed data.
6.	The measurement matrix satisfies the Restricted Isometry Property (RIP), enabling the accurate reconstruction of sparse or compressed data.
7.	The number of data sensed by the underwater node or aerial node is infinite.
8.	The sparsity of the data acquired by underwater nodes or aerial nodes varies over time and across different data types.
9.	The sensed signals are uniformly distributed in the sparse signal space, and there is no prior knowledge of their informational content.
10.	The spatial frequency of water waves is sparse.
11.	The environmental conditions remain constant during the simulation period, and rapid changes in their status do not occur.
12.	Environmental characteristics are homogeneously distributed throughout the air and water environment.
13.	In the simulation, atmospheric effects (including humidity, air pressure, etc.) were disregarded.

Table 2

Parameter settings in the simulations

Parameter		Value
Symbol	Description	
B	Electrical Bandwidth of the Photodetector	$100MHz$
θ_0	Beam Divergence Angle	$1° to 30°$
P_{ve}	Average Transmitter Optical Power	$25mW$
h	Depth of Receiver	$30m$
$\Delta\lambda$	Bandwidth of the Optical Filter	$10nm$
η_{al}	Optical Efficiency of the Receiver	0.9
T_F	Optical Filter Transmissivity	0.5
F	Noise Figure of the System	4
E	Downwelling Irradiance	$1440W / m^2$
L_{fac}	Factor Describing the Directional Dependence of the Underwater Radiance	$2.5(Horizontally)$
K_B	Boltzman Constant	$1.38\times10^{-23} J / K$
AL	Ambient Light	$450lx$
$CR_{Default}$	Default Compression Ratio	0.8164
$SX_{Default}$	Number of Nonzero Coefficients (Default Sparsity Level)	17
PW	Pulse Width	$10ns$
$P_{Acquisition}$	Sensing Power Consumption	$15.01mW$
$E_{SiPM\ Bias}$	Usage Energy of SiPM Bias	$25mW$
E_{Add}	Energy dissipation for addition	$3.3nj$
E_{Mul}	Multiplication Energy Dissipation	$9.9nJ$
$t_{Active\ Listening\ Period}$	Active Listening Period	$2.02s$
$\beta(\lambda)$	Scattering Coefficient	$1.3m^{-1}$
q	Elementary Charge	$1.6\times10^{-19} C$
$M_{Default}$	Number of Default Measurements	209
N	Total Number of Unknowns in R^N	256
$P_{Background}$	Background Power Consumption	$9.6mW$
E_{Pulse}	Pulse Energy	$0.12nJ$
$E_{Array\ Sensing}$	Usage Energy of Array Sensing	$623mW$
E_{Mrd}	Memory Read Energy Dissipation	$0.26nJ$
E_{Mwr}	Memory Write Energy Dissipation	$4.3nJ$
$t_{Instruction\ Execution}$	Instruction Execution Duration	$0.135\mu s$
$\alpha(\lambda)$	Absorption Coefficient	$0.9m^{-1}$

D	Aperture Diameter of Receiver	$1cm\,to\,50cm$
θ	Angle Between the Perpendicular to the Receiver Plane and the Transmitter Receiver Projection	$0°$
FOV	Field of View	$40°$
λ	Wavelength	$320nm$
η_{ve}	Optical Efficiency of the Transmitter	0.9
s	Sensitivity of the Photodetector	$0.35A/W$
R_L	Load Resistance of the Photodetector	100Ω
I_D	Dark Current	$1.226nA$
R	Underwater Reflectance of the Downwelling Irradiance	1.25%
T_K	Temperature	$290K$
θ_i	Initial Beam Angle	$\pm 5°\,in\,two\,\dim ensions$
ñ	Learning Rate	0.01
g	Earth's gravitational acceleration	$9.8m/s^2$
λ_w	Wavelength of water surface wave	$6.28m$
m	Elliptic modulus parameter	0.85
H	Wave height	$0.2m$

Biographies

Sobhan Esmaeili holding a Ph.D. (2020), MSc. (2016), and BSc. (2007) in Computer Networks from the Islamic Azad University, Central Tehran Branch, Tehran, Iran. He is serving as an Editorial Board Member and Reviewer for Several ISI Journals. He is also serving as a Postdoctoral Researcher at the Department of Computer and IT Engineering, Faculty of Technology and Engineering, Babolsar, Mazandaran, Iran. He has authored over 30 scientific research articles in ISI Journals, international journals and prestigious conferences. His research interests include IoT, Smart Healthcare, Covert Communication, and Computer and Telecommunication Networks.

Jamal Ghasemi received the M.Sc. and Ph.D. degrees from the Department of Electric and Computer Engineering, University of Mazandaran, Babolsar, Iran in 2008 and 2012, respectively. He is now associate professor in the University of Mazandaran, Babolsar, Iran. His research interests are mainly focused on the fuzzy and Dempster-Shafer theory, image and

signal processing, pattern recognition. He has authored more than 30 research papers and conference proceedings in the mentioned fields.